International Journal of Engineering

Journal Homepage: www.ije.ir

Design and Analysis of a Power Quality Improvement System for Photovoltaic Generation Based on LCL-Type Grid Connected Inverter

M. Hosseinpour*a, A. Dastgiria, M. Shahparastib

a Department of Electrical and Computer Engineering, University of Mohaghegh Ardabili, Ardabil, Iran
b School of Technology and Innovations, University of Vaasa, Vaasa, Finland

A B S T R A C T

Grid-connected inverters are considered vital elements for effectively connecting renewable energy sources and distributed generation system applications. Ripple-induced current harmonics in DC link and high switching frequency are the disadvantages of grid-connected inverters that are reduced by LCL filters. However, the intrinsic resonance in the LCL filter leads to instability of the power transmission system. As a result, suitable damping is essential for removing resonance in the LCL filters. The contribution of this paper is to improve the quality of injectable power of LCL filter-based grid-connected photovoltaic array. For this contribution, the stability of the grid-connected inverter has been investigated using active damping method, and maximum power point tracking (MPPT) for the PV array has been performed. The capacitor voltage feedforward active damping method considering computational delay is presented in this paper. By using the inverter-side current feedback beside this method, the proposed control maintains the system's low-frequency specifications independent of the grid impedance changes. It provides high harmonic rejection capability without additional compensators. Also, the number of sensors is decreased due to the alternative measurement of the capacitor voltage instead of the grid voltage for the phase lock loop (PLL). Meanwhile, maximum power point tracking is implemented using the incremental conductance (IC) technique in the boost converter. In addition, a simple and suitable computational method for designing LCL filter parameters is presented, and the system's sensitivity is analyzed. Finally, the simulation has been implemented in MATLAB software that indicates the accurate performance of the control system in injecting the maximum power of the photovoltaic array into the grid and the highly desirable quality of the injectable current to the grid.

doi: 10.5829/ije.2024.37.02b.04

Graphical Abstract
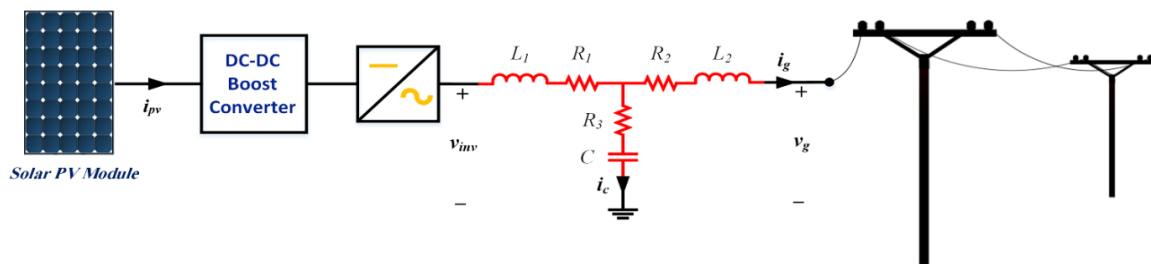
NOMENCLATURE

P_n	Nominal active power of the system (W)	f_s	Frequency in which Re(A) = 0
P_{pv}	Power of the photovoltaic array (W)	f_{res0}	Resonance frequency of the state in which the grid inductance is zero. (kHz)
v_g	Grid RMS line voltage (V)	f_{swR}	Actual value of switching frequency (kHz)

Corresponding Author Email: hoseinpour.majid@uma.ac.ir (M. Hosseinpour)

v_{pv}	Photovoltaic voltage (V)		f_g	Grid Frequency (Hz)
v_C	Capacitor voltage (V)		T_{sw}	Switching period
v_{L1}	Inveter-side inductor voltage (V)		T_{d1}	Forward path (control) delay time
v_{L2}	Grid-side inductor voltage (V)		T_{d2}	Feedforward path delay time
V_{inv}	Bridge voltage (V)		G_{d1}	Digital controller computation delay fuction
V_{dc}	Input DC voltage (V)		G_{d2}	Feedforward delay function
i_{pv}	Photovoltaic current (A)		G_Z	Zero-order hold (ZOH) function
i_{L1}	Inverter-side current (A)		G_{feed}	Feedforward coefficient
i_{L2}	Grid-side current (A)		λ_1	Forward path delay time to switching period ratio
I_{sat}	Saturation current of filter inductors (A)		λ_2	Feedforward path delay time to switching period ratio
L_1	Inverter-side inductor (μH)		$\varphi_{\_PI}$	PI controller phase angle at resonant frequency
L_2	Grid-side inductor (μH)		$\varphi_{\_delay}$	Total delay phase angle at resonant frequency
L_g	Grid inductor (μH)		ψ_1	Phase before the phase jump at resonant frequency
L_{20}	Designed inductor (μH)		ψ_2	Phase after the phase jump at resonant frequency
L_{2-C}	Grid-side inductor that can lead to a new resonance		K_{pwm}	Inverter gain
L_R	Actual value of inverter-side inductor		H_F	$G_{feed} * K_{pwm}$
C	Filter capacitor (μF)		C_e	Constant value
f_{sw}	Switching frequency (kHz)		δ	Harmonic attenuation rate
f_{res}	Resonance frequency (kHz)		m	Switching frequency to resonance frequency ratio
f_c	Control frequency (kHz)		k	Integer

1. INTRODUCTION

The microgrid (MG) concept arises from the use of distributed power generators and storage systems to meet demand for optimal operation, voltage/current control, and power quality (1). In the past decade, extensive installation of grid-connected renewable energy sources (RESs) increased including wind energy, solar photovoltaic energy (PV), biomass energy, tidal energy etc. (2). It is noteworthy that solar energy is installed faster and plays a vital role in electricity generation in some countries.

The photovoltaic array is a set of photovoltaic modules, composed of several interconnected cells. PV cells absorb the sun's radiant energy, leading to the current flow between the two layers with the opposite load. Due to the relatively low power generation of solar cells, cells, modules, and arrays can be connected in series or parallel, or in combination to achieve the desired peak output voltage. Electric vehicles, indoor and outdoor lighting, and water pumping can be powered by photovoltaic systems. Grid-connected applications include hybrid systems, power plants etc. (3).

Technological advances and increased production scale leads to continually decreased cost of the PV. PV systems are, however subjected to two fundamental problems, namely a low efficiency in converting solar energy into electrical energy, and a nonlinear design that results in a change in electrical energy produced based on temperature and sunlight (4).

The I-V and P-V curves of solar arrays reveal that to be the most efficient and produce maximum output power, a PV system can only operate at one maximum power point. Various algorithms are available for tracking the maximum power point (MPPT) position (5). It is possible to use several MPPT techniques, including perturbation and observation technique (P&O), incremental conductance technique (IC), ripple correlation technique, short circuit current technique (SCC), open circuit voltage technique (OCV) etc. There have been several reviews of these methods. The methods vary in complexity, cost, convergence speed, sensors required, hardware implementation, and effectiveness.

Inverter is the basic power converter for integrating solar photovoltaic sources with the grid, which converts DC power of the PV array into AC power for injection into the grid. So, the voltage source inverter (VSI) or current source inverter (CSI) is usually combined with DC/DC converter. However, a complex control structure is also needed to achieve better performance and optimal system output. The inverter plays a vital role in controlling the current injection into the grid. Hence, it maintains the voltage value of the DC link at an optimum level and controls the flow of active and reactive power to the grid (6). For this purpose, transformer-less grid-connected photovoltaic inverters are used due to their small size/weight, reduced cost, and high efficiency, which are preferable to inverters with transformers (7). To ensure that grid-connected photovoltaic inverters

comply with applicable laws and grid standards, grid-connected photovoltaic inverters should comply with grid standards (8, 9). Several electrical factors should be considered, including leakage current protection, grid frequency monitoring, active and reactive power control, and power quality.

Following IEEE 1547 standard, a filter is required to have a standard harmonic in the inverter output (10). The inductive filter L is one of the most straightforward filters leading to a simple controller design and practical implementation. In grid-connected inverters, LCL filters are preferred due to their high power density, low inductance, and better attenuation of switching frequency harmonics (11). The LCL filter has resonance despite having significant advantages that should be weakened by damping methods to maintain the stability of the inverter (12).

Researchers have proposed a wide range of approaches to address the concerns regarding the stability and injection quality of the LCL-based grid inverter (13). Adding resistance in series or parallel to the inductor or capacitor of the filter is a passive damping method that leads to reduced efficiency despite simplicity (14). Active damping is another method that attracted more attention due to low power loss. However, the high cost due to the number of elements added and the control complexity are the disadvantages of this damping method. The two main active damping methods are single and multi-loop damping methods. Each of these loops includes the capacitor voltage loop (15), the capacitor current loop (16-18), and other loops. It should be noted that single-loop control strategies are advantageous because they are simple and perform satisfactorily due to the absence of supplementary measurement methods or passive damping measures. Additionally, grid-connected inverters are typically controlled by two feedback nodes: a current feedback node on the grid-side inductor (grid-side current feedback) and a current feedback node on the inverter-side inductor (inverter-side current feedback).

A robust quasi-predictive control of LCL-filtered grid converters is applied (19). The proposed method provided the stability of the system against grid impedance changes. A control strategy with inverter-side current feedback-based active damping is proposed by Cai et al. (20), which is usually used to analyze the robustness of the control despite the design. An explanation of how to select the type of controller is not provided (20). A dual-current control method was proposed by Guan et al. (21) to improve the attenuation of resonances in grid-connected inverters with LCL filters. However, this strategy requires more sensors, which leads to an increase in the cost and complexity of the system. Based on negative resonance regulation and grid current feedback; Zhou et al. (22) presented a new active damping algorithm. The switching sensitivity of

this algorithm is lower, and the control delay compensation is higher. Using a combination of capacitor current feedback and point of common coupling voltage feedforward, a hybrid active damping algorithm is presented by He et al. (23). The association between these two damping methods ensures the robustness of the active damping in case of parameter change and non-ideal grid conditions. A grid-connected inverter control based on capacitor voltage damping using parallel feedforward compensation was presented by Faiz et al. (24), which uses an alternative feedforward path containing a second-order transfer function to improve system performance against grid impedance changes. Despite the proper stability of the system under investigation, the quality of the injected current to the grid has not been improved in an optimum way. A capacitor voltage feedforward control mechanism is used as part of the proposed approach by Li et al. (25), fully compensating for delays. In cases where the frequency of sampling is insufficiently high, or the analog-to-digital converter boasts high speed, this approach can be used to detect a sampling interval that is due to the computational delay. The effect of capacitor voltage feedforward was analyzed by Zou et al. (26) by considering variable computational delay through zero-pole graphs. Although the forward and feedforward path delays are considered equal despite being independent, in this case, accurate analysis is required. Thus, an accurate way to eliminate the resonance was proposed by Liu et al. (27), where the voltage of the capacitor is on the path of the feedforward. However, this method requires an accurate computational delay in the feedback loop, which creates a new resonance with the existence of an inappropriate delay. Capacitor voltage feedforward damping was applied by Figueredo and Matakas (28), in which the common-mode inductor is added towards AC/DC inverter to reduce the common-mode noise current. However, significant suppression would require a sizeable common-mode inductor, which violates the proposed method. A comparison between the capacitor voltage feedforward active damping and the notch filter for LCL-based grid-connected inverters with inverter-side current was proposed by Rodriguez-Diaz et al. (29). The preference for the capacitor voltage feedforward damping method is observable in the results regarding robustness in nominal conditions, stability in the weak grid, and desirable dynamic response.

A single-loop current control strategy based on active damping and an easy-to-use controller is presented in this paper, which has been applied to various industrial applications as well. Using inverter-side current control, the system is stable with a small computational delay. However, it becomes unstable with the increased computational delay in a limited period. By increasing computational delay, stability is again achieved. Unfortunately, the stable region with a limited

computational delay is considerably limited and decreases with increasing resonance frequency. Obviously, in this case, a high-speed processor is needed to detect the small delay time. Also, the delay is too short to fulfill the control codes for high frequency systems properly. Conversely, the region of stability showing enhanced computational delay is highly sensitive to changes in filter parameters. It may experience instability as a result of changes in grid impedance.

Hence, the main contributions of the current paper are as follows.
1. Improving the quality of injectable power of LCL filter-based grid-connected photovoltaic array.
2. Presenting the filter capacitor voltage feedforward with computational delay as a solution to overcome the aforementioned limitations and attenuation of resonance.
3. Developing the stability area of the system.
4. Removing the system sensitivity to grid impedance changes by applying the capacitor voltage feedforward. It is worth noting that the effect of computational delay on the stability of the system has also been investigated in both forward and feedforward paths, and the stability of the system has been significantly improved.
5. Providing high harmonic rejection capability without additional compensators.

Finally, the proposed system is combined with DC/DC boost converter. The injection power quality of the photovoltaic array connected to the LCL filter can be improved using the incremental conductance (IC) technique within the boost converter.

This paper is structured in the following manner; the analysis of the power quality improvement system for LCL-type PV grid-connected inverter is discussed in section two. In section three, an overview of the design and implementation of the LCL filter is provided. In section four, the implementation of the system using MATLAB simulation software is demonstrated and in the last part the paper is concluded with a brief conclusion.

2. SYSTEM ANALYSIS FOR IMPROVING POWER QUALITY OF GRID-CONNECTED PV INVERTER OF THE LCL TYPE:

Figure 1 illustrates the proposed system. The DC/DC boost converter and single-phase inverter based on the LCL filter connect the PV array to the grid.

2. 1. Incremental Conductance (IC) Technique Applied To DC/DC Boost Converter   Radiation and temperature changes, shading conditions, and nonlinear output power characteristics lead to fluctuation in the output power of the photovoltaic array. A DC/DC boost converter is proposed in this paper using the IC method to achieve the optimal duty cycle, thus improving injection power quality. MPPT is one of the most essential features of PV power systems. Hence, a DC/DC converter should be considered for MPPT implementation.

At the maximum power point, the slope of the PV array power curve is zero in the IC method $\Delta P/\Delta V = 0$, where $P = VI$. By considering Equation 1, the maximum power point is tracked by comparing the instantaneous conductance I/V with the incremental conductance $\Delta I/\Delta V$. The existing algorithm increases or decreases the reference value until the $\Delta I/\Delta V = -I/V$ condition is met. By achieving the maximum power point, PV array operations remain constant at the optimal point. Good efficiency tracking and automatic voltage regulation of the module without oscillation are the algorithm's advantages.

$$\frac{\Delta I}{\Delta V} = -\frac{I}{V} \ \ if \ \ P = MPP,$$
$$\frac{\Delta I}{\Delta V} > -\frac{I}{V} \ \ if \ \ P = MPP, \tag{1}$$
$$\frac{\Delta I}{\Delta V} < -\frac{I}{V} \ \ if \ \ P = MPP,$$

2. 2. System Stability With Inverter-Side Current Control and Feedforward Control of Capacitor Voltage

2. 2. 1. Strategy for Controlling the Inverter-Side Current   As shown in Figure 2, the current feedback control strategy for the inverter side is described. Digital controller computational delay indicates by G_{d1}.

$$G_{d1} = e^{-sT_{d1}} \tag{2}$$

The control imposed delay time denoted by the parameter T_{d1}. Furthermore, it is essential to note that the gain of K_{pwm} exhibits a value of V_{dc} when employed in a full-bridge inverter configuration, whereas, in a half-bridge inverter configuration, its gain is equal to $V_{dc}/2$. The mathematical model of the inverter is obtained according to the following Equation:

$$G_{PLANT}(s) = \frac{I_{L1}(s)}{V_{inv}(s)} = \frac{s^2 L_2 C + 1}{s^3 L_1 L_2 C + sL_1 + sL_2} \tag{3}$$

V_{inv} and I_{L1} denote the voltage across the bridge and the current flowing through the inverter side, respectively. Figure 3 illustrates the bode diagram of the G_{PLANT}. The phase undergoes a transition from a value of 90° to -90° at the resonant frequency, as can be seen. The resonant frequency is equal to:

$$f_{res} = \frac{1}{2\pi} \sqrt{\frac{L_1 + L_2}{L_1 L_2 C}} \tag{4}$$

The phase of the system before and after the phase jump at the resonant frequency is equal to:

Figure 1. Power circuit scheme of the power quality improvement system for LCL-type grid-connected PV by considering the control system

Figure 2. An inverter current feedback control strategy

Figure 3. Bode diagram of G_{PLANT}

$$\begin{cases} \psi_1 = 90° + \varphi_{\_delay} + \varphi_{\_PI} \\ \psi_2 = -90° + \varphi_{\_delay} + \varphi_{\_PI} \end{cases} \quad (5)$$

where the phase angles resulting from the total delay and the PI controller at the resonant frequency are represented by $\varphi_{\_delay}$ and $\varphi_{\_PI}$, respectively. It is important to note that the total delay includes the delay caused by the computation and the zero-order holding element (ZOH). Thus:

$$\varphi_{\_delay} = -f_{res}(T_{d1} + 0.5T_{sw}) \times 360° \quad (6)$$

It is worth noting that at high frequencies, the P controller can be used instead of a PI controller. In other words, $\varphi_{\_PI} \approx 0$ at the resonance frequency. If ψ_1 is within the range that appeared in Equation 7, the system is unstable.

$$-180° - 360°k < \psi_1 < 0° - 360°k \quad (7)$$

where k is an integer, it is worth mentioning that Equation 7 is a sufficient but unnecessary condition.

In the next step, some unstable areas are calculated. With the definitions of $m = f_{sw}/f_{res}$ and $\lambda_1 = T_{d1}/T_{sw}$ and replacing Equation 5 in Equation 7, the system becomes unstable under the following condition:

$$km + \frac{m-2}{4} < \lambda_1 < km + \frac{3m-2}{4} \quad (8)$$

Unstable areas are changed due to grid inductance changes, resonance frequency, and m. The stable and unstable regions can be seen in Figure 4 as per the formulation presented in Equation 8, and upon contemplation of the variation in the parameter m from a value of 3 to 5, with k set at 0. Therefore, three regions exist. Region I is stable and constrained. Region II is unstable. Region III is also stable if the m value rises to

three. However, as the grid inductance increases, the value of m increases, and the stability region approaches the unstable boundary.

2. 2. 2. Feedforward Control Strategy Using Capacitor Voltage
In order to maintain the stability of the system when taking into account the variation of the grid impedance, it is essential that the time delay T_{d1} be sufficiently small. In order to resolve this problem, the voltage feedforward method is used to resolve the slight computational delay in the control path. Unfortunately, the voltage feedforward method is impractical or requires a faster CPU. Therefore, the system's stability is then assessed following this method.

Since the capacitor voltage is measured simultaneously with the grid voltage for the Phase Locked Loop (PLL), there is no need to measure the capacitor voltage separately, which gives this method the advantage over other active damping methods. An illustrative depiction of the control methodology the utilization of capacitor voltage feedforward is presented in Figure 5. T_{d1} and T_{d2} are the delays in the forward and feedforward paths, respectively. G_{feed} is also called the feedforward coefficient. The delay relations in both paths are calculated as follows.

$$\begin{cases} G_{d1} = e^{-sT_{d1}} \\ G_Z = \dfrac{1}{T_{sw}}\dfrac{1-e^{-eT_{sw}}}{s} \approx e^{-0.5sT_{sw}} \\ G_{d2} = e^{-sT_{d2}} \end{cases} \tag{9}$$

By using capacitor voltage feedforward, the open loop transfer function of the system is calculated and can be seen in Equation 10:

$$GH(s) = \frac{\left(s^2 L_2 C + 1\right)G_{PI}G_{d1}G_Z K_{pwm}}{s^3 L_1 L_2 C + sL_1 + sL_2 - sL_2 G_{d2}G_{feed}G_z K_{pwm}} \tag{10}$$
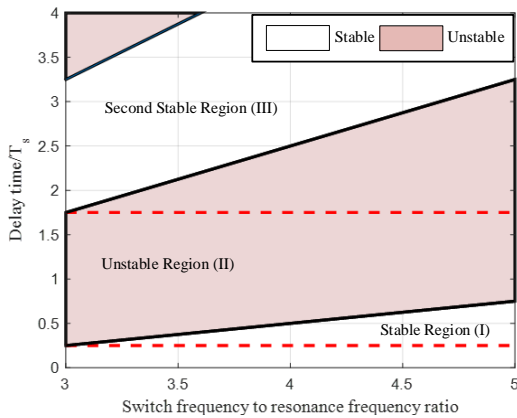
Figure 4. Regions with the varying resonant frequency

In the first step, it is necessary to determine the coefficient of the feedforward path using the characteristic Equation of the open loop transfer function, which is as follows:

$$s(s^2 L_1 L_2 C + L_1 + L_2 - L_2 G_{d2}G_{feed}G_z K_{pwm}) = 0 \tag{11}$$

Given that $|G_{d2}G_z| = 1$, the system will have no unstable open-loop pole if the Equation 12 is established.

$$G_{feed}K_{pwm} \le 1 \tag{12}$$

Under the assumption that the unit feedforward is a joint selection as well as the ideal feedforward in the context of the unit feedforward, G_{feed} can be calculated as follows:

$$G_{feed} = \frac{1}{K_{pwm}} \tag{13}$$

A quick check of the control and feedforward paths computation delays is conducted. Since feedforward control requires solely one additional operation, a very small value of T_{d2} can be chosen. However, T_{d1} caused by complex control codes cannot be as small as the computational delay T_{d2}. It is worth noting that the control frequency (f_c) can be equal to or twice the switching frequency (f_{sw}), which is considered equivalent in this article.

After examining the delay in the feedforward path by considering the non-ideal conditions, the G_{PLANT} function is changed to the modified function according to Equation 14.

$$G_P(s) =$$
$$\frac{s^2 L_2 C + 1}{s^3 L_1 L_2 C + sL_1 + sL_2 - sL_2 G_{d2}G_{feed}G_z K_{pwm}} \tag{14}$$

As a first step, the unit delay condition is analyzed in order to demonstrate the effect of the feedforward control strategy by taking into account the delay, where:

$$T_{d2} = T_{sw} \tag{15}$$

The bode diagram of $G_P(s)$ by considering the various resonance frequencies is shown in Figure 6. Based on the application of capacitor voltage feedforward, it is possible to summarize the different results in the following manner.
- Larger domain in low frequency
- Phase drop at low frequency without considering feedforward
- Elimination of the main positive resonance (However, producing a new resonance is possible whose phase drops by 180° around this resonance (according to Figure 6(b))

As a result, there is no significant difference between the feedforward path and without the feedforward path

for the $G_P(s)$ function to distinguish between these two paths.

By defining $G_{feed} * K_{pwm} = H_F$ where single feedforward and without feedforward identified by $H_F = 1$ and $H_F = 0$, respectively, the amplitude-frequency function of $G_P(s)$ can express according to Equation 16 where $\lambda_2 = T_{d2}/T_{sw}$.

$$G_{P\_MF} = \frac{1 - \omega^2 L_2 C}{-j\omega^3 L_1 L_2 C + j\omega L_1 + j\omega L_2 - jH_F \omega L_2 e^{-j(\lambda_2 + 0.5)\omega T_{sw}}}$$
$$= \frac{1 - \omega^2 L_2 C}{\omega} \frac{1}{A} \tag{16}$$

Considering the unit delay, $\lambda_2 = 1$.

$$A = -H_F L_2 \sin 1.5\omega T_{sw}$$
$$+ j(L_1 + L_2 - \omega^2 L_1 L_2 C - H_F L_2 \cos 1.5\omega T_{sw}) \tag{17}$$

$L_1 + L_2 - \omega^2_{res} L_1 L_{20} C = 0$ at the resonance frequency. G_P domain in f_{res} is equal to :

$$|G_P| = \frac{1}{H_F \omega_{res} L_1} \tag{18}$$

Therefore, there is an infinite resonance in the value of $H_F = 0$, which will be removed if the two conditions $H_F = 1$ and $\omega_{res} L_1 > 1$ are established. As can be seen, the G_P domain in f_{res} has a reverse relation with H_F, ω_{res}, and L_1. However, it is possible to create a new resonance at this time.

The condition that limits this, is the equality of the real and imaginary part of the expression A with zero value at the same frequency.

$$\text{Re}(A) = \text{Im}(A) = 0 \tag{19}$$

$Re(A) = 0$ occurs when

$$f_s = \frac{k f_{sw}}{3}, \quad k = 0, 1, 2, \ldots \tag{20}$$

f_s is the frequency that causes the real value of A to become zero. Also, $k = 0$ is meaningless due to the representation of the dc signal and does not affect the infinite gain in the dc signal system stability. It is worth mentioning that the possibility of creating an infinite resonance peak is provided by $Im(A)$ becoming zero at f_s.
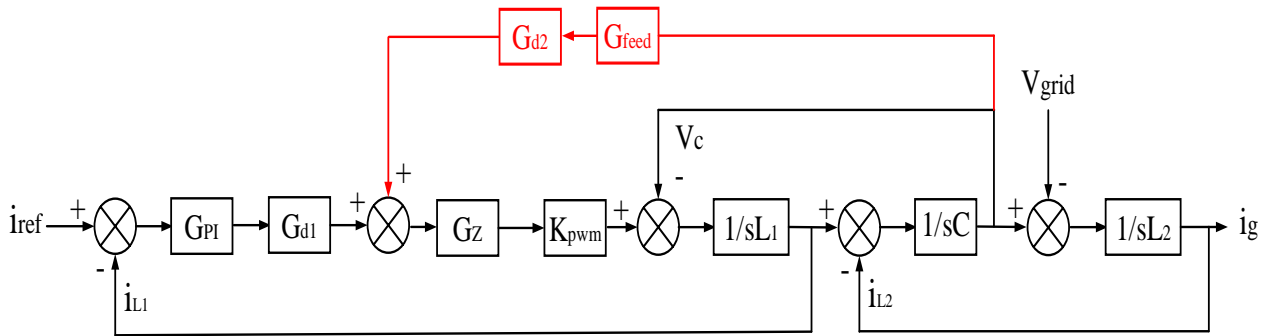
Figure 5. Capacitor voltage feedforward control strategy
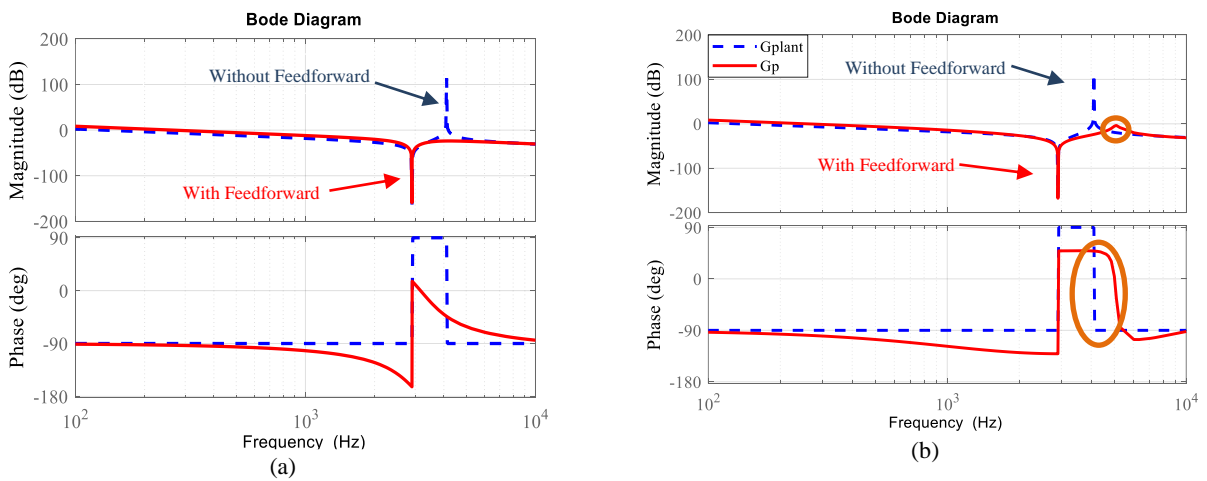
Figure 6. $G_P(s)$ bode Diagram with various resonance frequencies (a) Without resonance status (b) With new resonance status

In addition, the finite resonance peak is created with low $Im(A)$ in the f_s. Similarly, if the $Im(A)$ value in the f_s is large enough, no new resonance peak will occur. However, if Equation 20 is replaced by Equation 17, then a new resonance peak will occur as follows:

$$L_1 + L_2 - 4\pi^2 L_1 L_2 C \frac{k^2 f_{sw}^2}{9} - (-1)^k L_2 = 0 \qquad (21)$$

By solving Equation 21, a new component for the grid side inductor can define (L_{2-C}), which leads to a new resonance. Hence, a new infinite resonance will exist, by equalization of the LCL filter grid-side inductor with the following value.

$$L_{2-C} = \frac{L_1}{4\pi^2 L_1 C \frac{k^2 f_{sw}^2}{9} + (-1)^k - 1} \qquad (22)$$

It is worth noting that a smaller value of the L_{2-C} than the value of the grid-side inductor L_2 will prevent the existence of a new infinite resonance. So, an inverter with zero grid equivalent inductor has the minimum grid-side inductor, theoretically L_{20}. On the other hand, the $k = 1$ means a maximum value of L_{2-C}. Therefore, only $k = 1$ state is considered.

Finally, it can be concluded that there will be an infinite resonance if L_{2-C} is greater than L_{20}. Therefore, there will be a new resonance if

$$L_{2-C} = \frac{L_1}{4\pi^2 L_1 C \frac{f_{sw}^2}{9} - 2} > L_{20} \qquad (23)$$

The $L_1 + L_{20} - 4\pi^2 f_{res0}^2 L_1 L_{20} C = 0$ can now be placed in Equation 23 and resolved that the final condition is obtained according to the following Equation 24.

$$L_{20} < \frac{L_1 \left(\frac{f_{sw}^2}{9 f_{res0}^2} - 1 \right)}{\left(2 - \frac{f_{sw}^2}{9 f_{res0}^2} \right)} \qquad (24)$$

where f_{res0} is the resonant frequency of the state in which the grid inductance is zero. According to Equation 24, when f_{res0} is between the values of $0.235 f_{sw}$ and $0.333 f_{sw}$, L_{20} has a positive value. Also, a new infinite resonance can occur by adopting the unit feedforward.

The infinite resonance peak occurs with the equality of $(L_2 = L_{2-C})$, which can be seen in the following Equation.

$$L_{2-C} = L_2 = \frac{L_1 \left(\frac{f_{sw}^2}{9 f_{res}^2} - 1 \right)}{\left(2 - \frac{f_{sw}^2}{9 f_{res}^2} \right)} \qquad (25)$$

However, such a state is extraordinary and difficult to establish. Therefore, the resonance peak value is essential when L_2 is around L_{2-C}. The gain is shown by calculating the G_P amplitude when the grid inductance changes around L_{2-C}.

A variable describing the ratio between the resonance frequency and the switching frequency (f_{res}/f_{sw}) and the (L_2/L_1) ratio is utilized in arrange to maintain a strategic distance from employing a particular illustration to demonstrate the alteration in resonance phenomenon. The amplitude is calculated according to Equation 26. It can be seen that there is a term of $(f_{sw}L_1)$ in Equation 26, which is a constant term and has no effect on the inclination of resonance peak changes.

$$|G_P| = \frac{1}{f_{sw}L_1} \times \left| \frac{1 - \left(1 + \frac{L_2}{L_1}\right) \frac{f^2}{f_{sw}^2} \frac{f_{sw}^2}{f_{res}^2}}{2\pi \frac{f}{f_{sw}}} \right|$$
$$\times \frac{1}{\sqrt{\left(\frac{L_2}{L_1} \sin \frac{3\pi f}{f_{sw}}\right)^2 + \left(\left(1 + \frac{L_2}{L_1}\right)\left(1 - \frac{f^2}{f_{sw}^2} \frac{f_{sw}^2}{f_{res}^2}\right) - \frac{L_2}{L_1} \cos \frac{3\pi f}{f_{sw}}\right)^2}} \qquad (26)$$

G_P resonance peak is analyzed assuming $f_{sw} = 10kHz$ and $L_1 = 1mH$. The new resonance peak can be accomplished by means of choosing different values for the actual value of the inverter side inductor and the switching frequency (L_R, f_{swR}), and adding a constant value of C_e. The constant value of C_e is equal to

$$C_e = 20 \times \lg \frac{f_{sw}L_1}{f_{swR}L_R} \qquad (27)$$

G_P resonance peak can be calculated through MATLAB software considering specific values for (f_{res}/f_{sw}) and (L_2/L_1). It is worth noting that λ_2 is considered equal to one in all the above relations, which can be assumed as a variable. By reducing the computational delay λ_2 and reducing the maximum value of L_{2-C}, the limitation of the grid-side inductor is also reduced.

Next, the design of the LCL filter is analyzed, and appropriate values are obtained for each element.

3. DESIGN OF LCL FILTER

The grid-side inductor includes the equivalent grid inductor and designed inductor under the following relation in the single-phase inverter system described in Figure 1.

$$L_2 = L_g + L_{20} \qquad (28)$$

L_g is the grid equivalent inductor, and L_{20} is the designed inductor. L_1 and C, shown in Figure 1, are also called inverter-side inductor and filter capacitor, respectively.

It attempts to meet the grid code requirements by attenuating high-order harmonics on the grid side by

using LCL filters (30). The following input data are required to design the LCL filters:

- Grid RMS line voltage V_g
- Nominal active power of the system P_n
- Nominal frequency of grid voltage f_g
- Converter switching frequency f_{sw}
- Saturation current of filter inductors I_{sat}

Then the LCL filter parameters are adjusted according to the following steps.

3. 1. Total Inductor Maximum Value   To prevent losses and filter voltage drops, it is recommended to consider the sum of LCL filter inductor values as small as possible. The total inductance value should be less than 0.1 per unit to improve the system's speed and dynamics.

$$L_{T\max} = \left(L_1 + L_2\right)_{\max} = 10\% L_{TBase} \tag{29}$$

$$\begin{cases} L_{TBase} = \dfrac{Z_{Base}}{2\pi f_g} \\[2mm] Z_{Base} = \dfrac{V_g^2}{P_n} \end{cases} \tag{30}$$

$$L_{T\max} = 10\% \frac{V_g^2}{2\pi f_g P_n} \tag{31}$$

Here, L_{TBase} is the base value of the total inductor, and Z_{Base} is the base impedance.

3. 2. LCL Filter Capacitor With a Maximum Value The power consumed by the capacitor Q_C should be 2% to 5% of the nominal power injected into the grid. For this purpose, the selection range of the capacitor is determined as follows:

$$\begin{cases} C_f \le \dfrac{5\% P_n}{2\pi f_g V_g^2} \\[2mm] C_f \ge \dfrac{2\% P_n}{2\pi f_g V_g^2} \end{cases} \tag{32}$$

An additional point to note is that when the capacitor amount is low, it is recommended to select very high inductor values. To achieve satisfactory results, it is recommended to start with a capacitor value equal to half of the maximum value and increase it to the maximum value if it is unsatisfied.

3. 3. Adjustment of Inverter Side Inductor   In the most severe case where the ripple current originates from the pulse voltage produced by the converter, the inductor on the inverter side of the converter is designed

to reduce the ripple current.

$$\begin{aligned} V_{i\max} &= \sqrt{V_{g\max}^2 + \left(L_{T\max}\left(2\pi f_g\right)I_{2\max}\right)^2} \\[1mm] V_{dc\min} &= \sqrt{2}\,V_{i\max} \\[1mm] I_{1\max} &= \frac{P_n}{V_g} \\[1mm] I_{sat} &= 20\% I_{2\max} \end{aligned} \tag{33}$$

Finally, L_{imin} is equal to

$$L_{1\min} > \frac{V_{dc}}{16 f_{sw}\left(I_{sat} - I_{1\max}\right)} \tag{34}$$

It is noteworthy that the value of L_{imin} should be smaller than the value of L_{Tmax}.

$$L_{1\min} \le L_{T\max} \tag{35}$$

3. 4. Adjustment of Grid Side Inductor   Depending on a grid code standard and requirements, the grid side inductor should limit grid current harmonics compared to the IEEE519-1992 standard. This provides a total harmonic disturbance (THD) limit of less than 5% for grid currents.

Following is a formula that calculates the relation between the inductor on the inverter side and the inductor on the grid side.

$$L_2 = a L_1 \tag{36}$$

where

$$0 \le a \le a_{\max} \;\rightarrow\; a_{\max} = \frac{L_{T\max}}{L_1} - 1 \tag{37}$$

The harmonic attenuation rate δ is used to determine the coefficient a, which represents the relation between the currents on the inverter and grid sides at the switching frequency. The relation between these two coefficients is:

$$a = \frac{1+\delta}{\delta a_1} \;\rightarrow\; a_1 = L_1 C_f \omega_{sw}^2 - 1 \tag{38}$$

A proper design should take into account the following conditions for harmonic attenuation rate:

$$\begin{cases} \delta > \dfrac{36 L_1 - (2\pi f_{sw} L_1)^2 C_{f\max}}{a_3 (2\pi f_{sw})^2 - 36 a_2} \Rightarrow 1^{st}\,\delta\ condition \\[3mm] \delta < \dfrac{4 L_1 - (2\pi f_{sw} L_1)^2 C_{f\min}}{b_3 (2\pi f_{sw})^2 - 4 b_2} \Rightarrow 2^{nd}\,\delta\ condition \end{cases} \tag{39}$$

The unknown coefficients of Equation 39 are calculated according to the following relations:

$$\begin{cases} a_1 = L_1 C_f \left(2\pi f_{sw}\right)^2 - 1 \\ a_2 = L_1 + a_1 L_{g\,max} + a_1 L_1 \\ a_3 = \left(L_1 + a_1 L_{g\,max}\right) L_1 C_{f\,max} \end{cases} \tag{40}$$

$$\begin{cases} b_2 = L_1 + a_1 L_{g\,min} + a_1 L_1 \\ b_3 = \left(L_1 + a_1 L_{g\,min}\right) L_1 C_{f\,min} \end{cases}$$

In addition, to ensure the change of resonance frequency in the stability region, the desired harmonic attenuation rate must be greater than the minimum harmonic attenuation rate δ_{min}, which corresponds to a_{max}.

$$\delta > \delta_{min} = \frac{1}{\left|1 + a_{max} a_1\right|} \Rightarrow 3rd\ \delta\ condition \tag{41}$$

It is worth noting that the current harmonics will decrease by decreasing the value of δ. The harmonic disturbance of the total grid current is also reduced by reducing the harmonic attenuation rate of δ. The desired harmonic attenuation rate may be easily determined by applying Equations 39-41. As a next step, the value of coefficient a is determined by utilizing Equation 38, and finally, the value of the grid side inductor is determined by utilizing Equation 36.

$$f_{res} = \frac{1}{2\pi} \sqrt{\frac{L_1 + L_2}{L_1 L_2 C_f}}$$

$$10 f_g \leq \frac{f_{sw}}{6} \leq f_{res} \leq 0.5 f_{sw} \tag{42}$$

4. SIMULATION RESULTS

In this section, to verify the performance of the inverter side inductor current feedback technique and the proposed filter capacitor voltage feedforward, the PV array system grid-connected single-phase inverter is simulated in MATLAB software, and the results are discussed in detail. Tables 1 and 2 present a list of parameters used for each system.

The stability of the proposed system has been investigated under five different scenarios, which are:
- Scenario 1: Stable condition
- Scenario 2: Sudden changes in solar radiation
- Scenario 3: Grid voltage drop condition (sag)
- Scenario 4: Grid voltage increase condition (swell)
- Scenario 5: Applying the fifth and seventh harmonics

Figure 7 shows the I-V and P-V curves of the SunPower SPR-E20-327 solar array for two different radiation intensities, 1000 W/m^2, and 800 W/m^2, respectively. In the radiation of 1000 W/m^2, the current of the solar array is equal to 94.17 A, and the voltage is equal to 2.328 V. It is worth mentioning that the

TABLE 1. Parameters used in the simulation

Parameter	Symbol	Value
Grid Voltage and Frequency	(V_g, f_g)	230 V, 50 Hz
Boost Switching Frequency	$(f_{sw,B})$	5 kHz
Inverter Switching Frequency	(f_{sw})	10 kHz
Boost Inductor	(L_B)	5 mH
DC-Link Capacitor	(C_{dc})	6 μF
Inverter Side Inductor	(L_1)	600 μH
Grid Side Inductor	(L_2)	265 μH
Grid Equivalent Inductor	(L_g)	550 μH
Filter Capacitor	(C)	8 μF
Controller Parameters	(k_P, k_i)	1, 4500
Capacitor Voltage Feedforward Coefficient	(H_{i1})	0.005
Inverter Side Current Inductor Feedback Coefficient	(H_{i2})	0.15

TABLE 1. PV Panel Parameters (With 25˚C Temperature and 1000 W/m^2 Radiation Intensity)

Parameter	Symbol	Value
Open Circuit Voltage	(v_{oc})	65.1 V
Maximum Voltage	(v_{mp})	54.7 V
Short Circuit Current	(i_{sc})	6.46 A
Maximum Current	(i_{mp})	5.98 A
Maximum Power	(P_m)	327.106 W
Number of Series Panels	(N_s)	6
Number of Parallel Panels	(N_p)	3

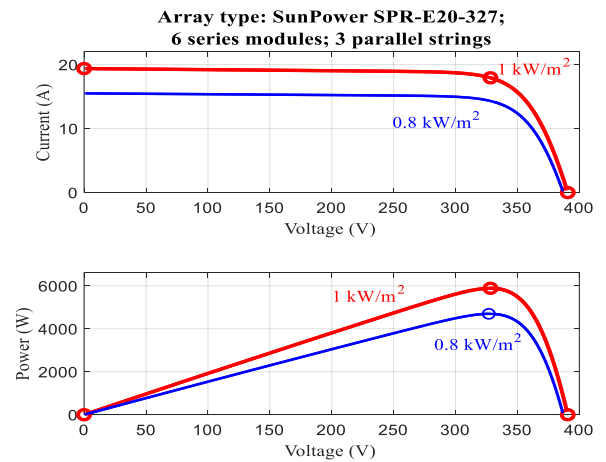maximum power of the PV array is equal to 5888 W. Now different scenarios will be examined.

Figure 7. I-V and P-V curve of the solar array

The four mentioned scenarios define different disturbances caused by PV and single-phase grid. During these scenarios, dynamic performance such as grid voltage V_g, grid current I_{L2}, grid power P_g, and grid current THD are evaluated to check grid condition. Also, the dynamic behavior of v_{pv}, i_{pv}, P_{pv}, and V_{dc} are investigated to analyze the PV performance during different test scenarios.

Scenario 1: In Figures 8-10, the dynamic behavior of the PV system connected to the grid with a single-phase inverter is investigated in stable conditions.

PV current and voltage are depicted in Figures 8(a) and 8(b). The current and voltage equal 18.7 A and 305 V, respectively. The maximum power of the solar array can also be seen in Figure 8(c), which is equal to 5620 W. Notably, the simulation results have little difference

Figure 9. DC-Link capacitor voltage under stable condition

from the expected values. The DC link capacitor voltage of the boost converter output is represented in Figure 9, which tracks the reference voltage $V_{dc} = 500$ V very well. The waveform of the current injected into the grid can also be seen in Figure 10(a), which shows the injection of sinusoidal current into the grid well. Figure 10(b) shows the grid voltage and current waveforms. The grid voltage and current waveforms are completely sinusoidal, with no phase difference between voltage and current. The injected power to the grid is also shown in Figure 10(c), which is equal to 5620 W according to the PV array production power. Finally, the grid current THD is shown in Figure 11, equal to 0.78%.

Scenario 2: In Figures 12-15, the dynamic behavior of the PV system connected to the grid with a single-

Figure 8. PV output graphs under stable conditions. a) PV output current b) PV output voltage c) PV output power

(c)
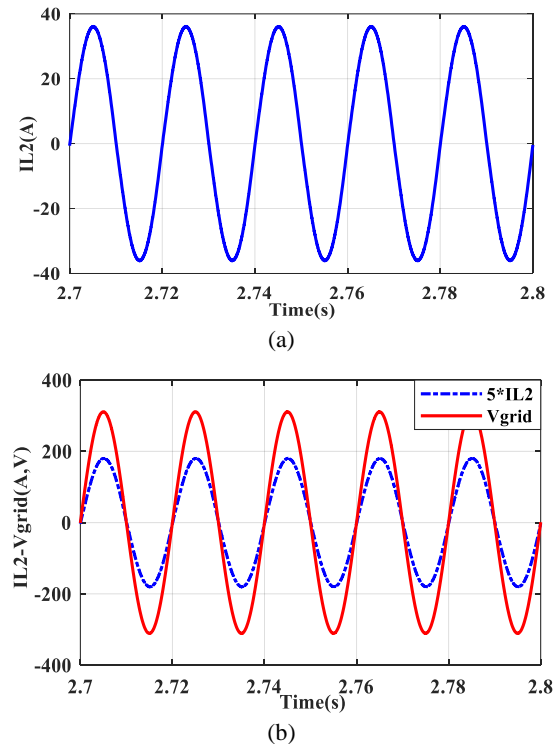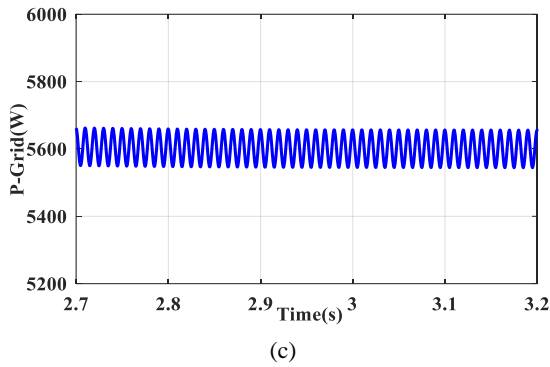
Figure 10. Dynamic performance of PV power injection system in stable condition. a) grid current b) grid current and voltage c) grid power
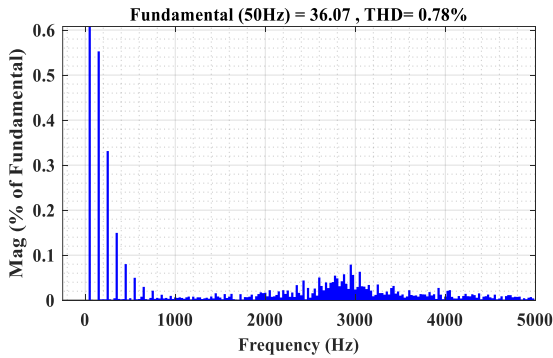

Figure 11. Grid current THD under stable condition

phase inverter was investigated in the solar radiation intensity sudden change condition. The radiation intensity decreases from 1000 W/m^2 to 800 W/m^2 in 3.3-3.9 seconds. In the 800 W/m^2 radiation, the current of the solar array is equal to 14.37 A, and the voltage is equal to 326.9 V. It is worth mentioning that the maximum power of the PV array is equal to 4698W.

The PV current increases or decreases depending on sudden changes in solar radiation, as shown in Figure 12(a). As shown in Figure 12(b), a slight change in PV voltage occurs during this scenario to achieve maximum power. The power produced by the solar array during the decreasing radiation intensity is also shown in Figure 12(c), which decreases from 5620 watts to 4450 watts with a slight difference compared to the P-V curve in Figure 7 and then increases.

The slight difference between the obtained results with the values of the curves in Figure 7 confirms the accuracy of the simulation. The DC link capacitor voltage can be seen in Figure 13. Due to the effect of the incremental conductance technique and the applying MPPT, the DC link voltage adaptively maintains a constant value of 500 V. The grid current THD is shown in Figure 14, whose value equals 1.02%.

Figure 15(a) shows the injection of current into the grid. There is a corresponding decrease in the injection current to the grid during the radiation reduction period. A return to its initial level follows this point. Figure 15(b) shows the injection current in phase with the grid voltage while the radiation reduction period. The grid power during decreasing radiation intensity is also shown in Figure 15(c). The change in the power value is according to the production power of the PV array.

Scenario 3: In Figure 16, the dynamic behavior of the PV system connected to the grid with a single-phase inverter under grid voltage drop (sag) is examined during 3.1-3.35 seconds when the grid voltage is reduced by 20%. The grid current increment under the grid voltage reduction, the in-phase current and grid voltage, and the sinusoidal shape of the grid current can be seen in Figure 16.
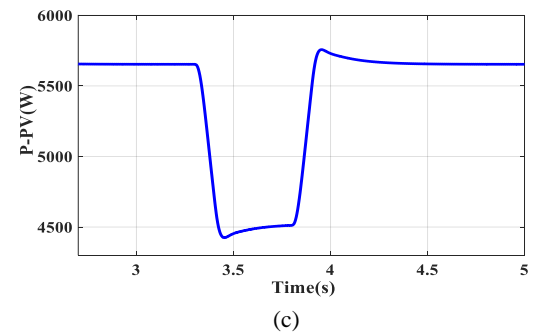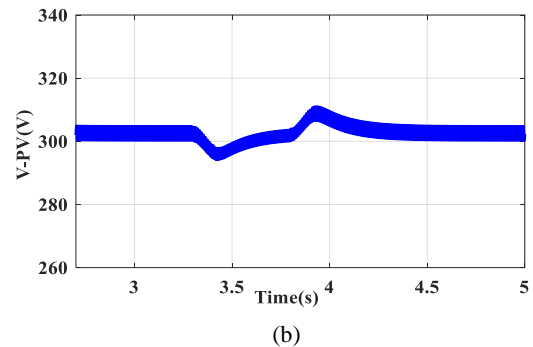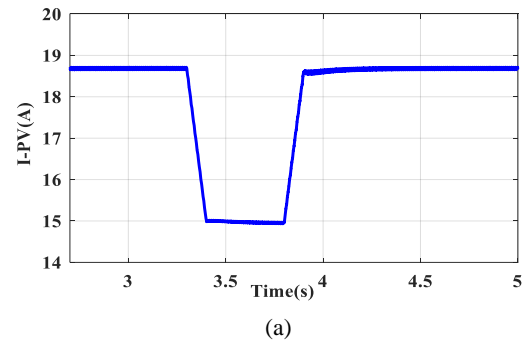

(a)

(b)

(c)

Figure 12. PV output graphs under sun radiation intensity sudden change condition. a) PV output current b) PV output voltage c) PV output power
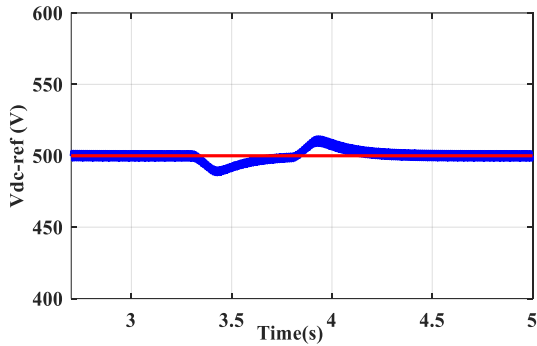
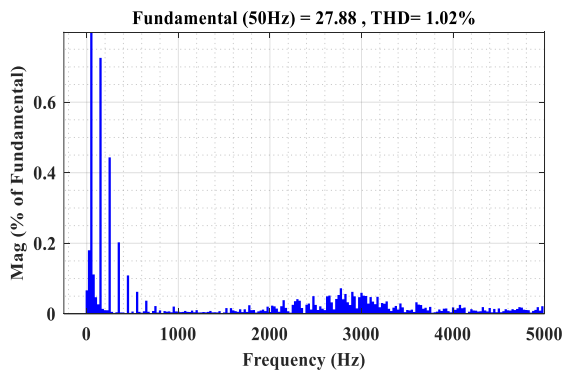**Figure 13.** DC-Link capacitor voltage under sun radiation intensity sudden change condition

Figure 14. Grid current THD under sun radiation intensity sudden change condition
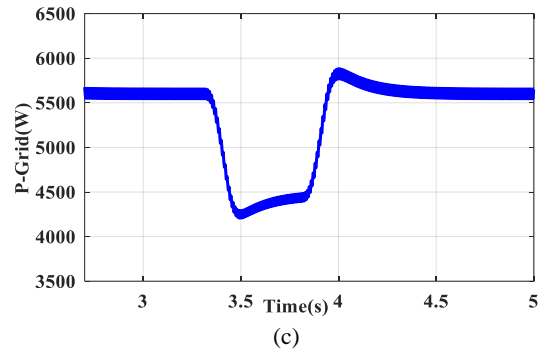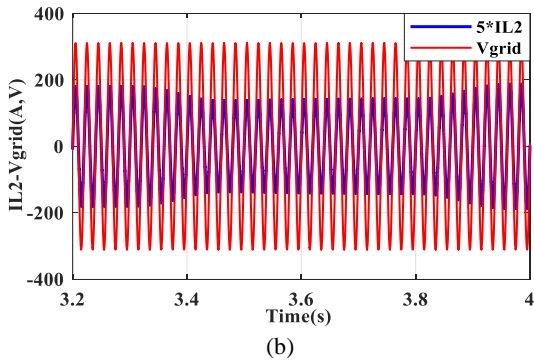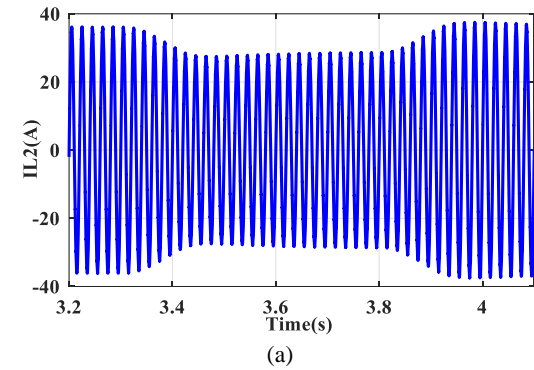

(a)

(b)

(c)

Figure 15. Dynamic performance of PV power injection system under sun radiation intensity sudden change condition. a) grid current b) grid current and voltage c) grid power
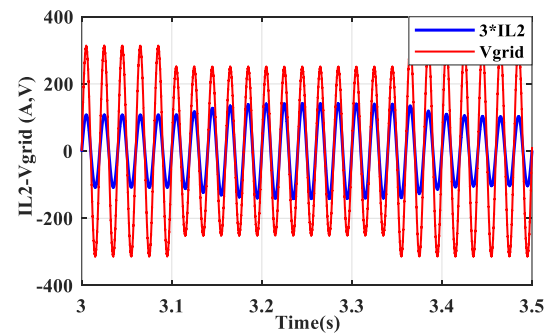

Figure 16. Dynamic performance of PV power injection system under grid voltage drop (sag) condition. Grid current and voltage

Scenario 4: In Figure 17, the dynamic behavior of the PV system connected to the grid with a single-phase inverter under the condition of the grid voltage increment (swell) in the period 3.10-3.35 seconds is examined when the grid voltage increases by 10%. The grid current drop under the rise of grid voltage, and the in-phase current and grid voltage can be seen in Figure 17.
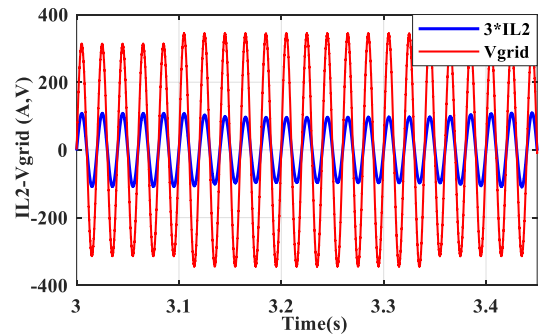

Figure 17. Dynamic performance of PV power injection system under grid voltage increment (swell) condition. Grid current and voltage

Scenario 5: A single-phase inverter is used in this scenario to connect a PV system to the grid, and fifth and seventh harmonics are applied to the system to determine its dynamic behavior. Figure 18 illustrates the grid voltage and current, which have fifth and seventh harmonics, with the in-phase voltage and grid current remaining unchanged. Notably, under grid voltage drop, the THD of the grid current remains below 5% according to the IEEE-519 standard, which can be seen in Figure 19.

Finally, the comparison of the proposed damping method with the current methods that is made in the area of enhancing the performance of the grid-connected inverter control system is presented in Table 3. The compared references are evaluated in terms of control strategy, filter design, and control delay. Moreover, the THD value of the current injected into the grid under the assumed conditions of this paper is also presented in Table 3. It is worth mentioning that the aim of presenting the THD value is only to show a comprehensive comparison. Whereas the different conditions considered in each reference lead to the uncited comparison of the harmonic values with each other. It is obvious that except for data reported by Cai et al. (20), the current injected
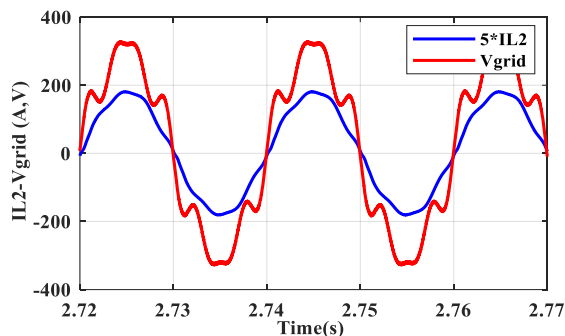
TABLE 3. Comparison of the proposed method with recent published articles

Ref.	Control Strategy	Filter Design	Grid Side Sensors Count	THD Value
[19]	Capacitor Voltage Feedback	X	3	2.62%
[20]	Inverter Side Current Feedback	X	3	0.38%
[21]	Inverter & Grid Side Current Feedbacks	X	3	3.02%
[22]	Grid Side Current Feedback	X	2	2.3%
[23]	Capacitor Current Feedback & Common Coupling Voltage Feedforward	X	3	2.2%
[24]	Quasi-Predictive Control	X	3	4.35%
Proposed	Capacitor Voltage Feedforward & Inverter Side Current Feedback	☑	2	0.78%

into the grid using the proposed approach has a lower THD and a higher quality than the others. The number of filters utilized in the grid side indicates that the proposed scheme uses lower number of filters versus most of compared schemes resulting in lower sensor cost.

5. CONCLUSION

In this article, a grid-connected PV array system with a LCL filter-based single-phase inverter is proposed. Improving the dynamic performance of the control system without adding power losses and improving the quality of injected power of the photovoltaic array connected to the grid are among the aims of the proposed system.

In this article, the filter capacitor voltage feedforward is used along with the inverter side current feedback, which leads to increasing the stability of the system. In addition, the LCL filter resonance is also damped by the presented control methods. As a result of the MATLAB simulation software, the stability of the system is demonstrated under different scenarios, which confirms the accuracy of the content presented in this article.

Figure 18. Grid voltage and current under fifth and seventh harmonics
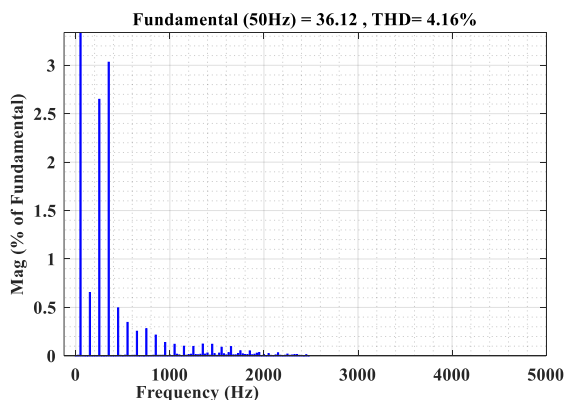
Figure 19. Grid current THD under fifth and seventh harmonics

6. ACKNOWLEDGMENT

6. REFERENCES

1. Mobashsher MM, Keypour R, Savaghebi M. Distributed optimal voltage control in islanded microgrids. International Transactions on Electrical Energy Systems. 2021;31(11):e13045. 10.1002/2050-7038.13045

2. Sagar G, Debela T. Implementation of optimal load balancing strategy for hybrid energy management system in dc/ac microgrid with pv and battery storage. International Journal of Engineering, Transactions A: Basics. 2019;32(10):1437-45. 10.5829/ije.2019.32.10a.13

3. Manna S, Singh DK, Akella AK, Kotb H, AboRas KM, Zawbaa HM, et al. Design and implementation of a new adaptive MPPT controller for solar PV systems. Energy Reports. 2023;9:1818-29. 10.1016/j.egyr.2022.12.152

4. Tang C-Y, Wu H-J, Liao C-Y, Wu H-H. An optimal frequency-modulated hybrid MPPT algorithm for the LLC resonant converter in PV power applications. IEEE Transactions on Power Electronics. 2021;37(1):944-54. 10.1109/TPEL.2021.309467

5. Hooshmand M, Yaghobi H, Jazaeri M. Irradiation and Temperature Estimation with a New Extended Kalman Particle Filter for Maximum Power Point Tracking in Photovoltaic Systems. International Journal of Engineering, Transactions C: Aspects,. 2023;36(6):1099-113. 10.5829/ije.2023.36.06c.08

6. Zeb K, Khan I, Uddin W, Khan MA, Sathishkumar P, Busarello TDC, et al. A review on recent advances and future trends of transformerless inverter structures for single-phase grid-connected photovoltaic systems. Energies. 2018;11(8):1968. 10.3390/en11081968

7. Giacomini JC, Michels L, Cavalcanti MC, Rech C. Modified discontinuous PWM strategy for three-phase grid-connected PV inverters with hybrid active–passive damping scheme. IEEE Transactions on Power Electronics. 2019;35(8):8063-73. 10.1109/TPEL.2019.2961648

8. Bharath GV, Hota A, Agarwal V. A new family of 1-φ five-level transformerless inverters for solar PV applications. IEEE Transactions on Industry Applications. 2019;56(1):561-9. 10.1109/TIA.2019.2943125

9. Guo X, Yang Y, Wang B, Blaabjerg F. Leakage current reduction of three-phase Z-source three-level four-leg inverter for transformerless PV system. IEEE Transactions on Power Electronics. 2018;34(7):6299-308. 10.1109/TPEL.2018.2873223

10. Hosseinpour M, Rasekh N. A single-phase grid-tied PV based trans-z-source inverter utilizing LCL filter and grid side current active damping. Journal of Energy Management and Technology. 2019;3(3):67-77. 10.22109/jemt.2019.169380.1150

11. Aalizadeh F, Hosseinpour M, Dejamkhooy A, Shayeghi H. Two-stage control for small-signal modeling and power conditioning of grid- connected quasi-Z-Source inverter with LCL filter for photovoltaic generation. Journal of Operation and Automation in Power Engineering. 2021;9(3):242-55. 10.22098/joape.2021.7674.1546

12. Wu W, Liu Y, He Y, Chung HS-H, Liserre M, Blaabjerg F. Damping methods for resonances caused by LCL-filter-based current-controlled grid-tied power inverters: An overview. IEEE Transactions on Industrial Electronics. 2017;64(9):7402-13. 10.1109/TIE.2017.2714143

13. Rasekh N, Hosseinpour M. LCL filter design and robust converter side current feedback control for grid-connected Proton Exchange Membrane Fuel Cell system. International Journal of Hydrogen Energy. 2020;45(23):13055-67. 10.1016/j.ijhydene.2020.02.227

14. Giacomini JC, Michels L, Pinheiro H, Rech C. Design methodology of a passive damped modified LCL filter for leakage current reduction in grid-connected transformerless three-phase PV inverters. IET Renewable Power Generation. 2017;11(14):1769-77. 10.1049/iet-rpg.2017.0256

15. Dannehl J, Fuchs FW, Thøgersen PB. PI state space current control of grid-connected PWM converters with LCL filters. IEEE transactions on power electronics. 2010;25(9):2320-30. 10.1109/TPEL.2010.2047408

16. Liu J, Zhou L, Molinas M. Damping region extension for digitally controlled LCL-type grid-connected inverter with capacitor-current feedback. IET Power Electronics. 2018;11(12):1974-82. 10.1049/iet-pel.2018.0039

17. Rasekh N, Rahimian MM, Hosseinpour M, Dejamkhooy A, Akbarimajd A, editors. A step by step design procedure of PR controller and capacitor current feedback active damping for a LCL-type grid-tied T-type inverter. 2019 10th International Power Electronics, Drive Systems and Technologies Conference (PEDSTC); 2019: IEEE. 10.1109/PEDSTC.2019.8697853

18. Hosseinpour M, Asad M, Rasekh N. A step-by-step design procedure of a robust control design for grid-connected inverter by LCL filter in a weak and harmonically distorted grid. Iranian Journal of Science and Technology, Transactions of Electrical Engineering. 2021;45:843-59. 10.1007/s40998-021-00414-z

19. Dragičević T, Zheng C, Rodriguez J, Blaabjerg F. Robust quasi-predictive control of $ LCL $-filtered grid converters. IEEE Transactions on Power Electronics. 2019;35(2):1934-46. 10.1109/TPEL.2019.2916604

20. Cai Y, He Y, Zhou H, Liu J. Active-damping disturbance-rejection control strategy of LCL grid-connected inverter based on inverter-side-current feedback. IEEE Journal of Emerging and Selected Topics in Power Electronics. 2020;9(6):7183-98. 10.1109/JESTPE.2020.3017678

21. Guan Y, Wang Y, Xie Y, Liang Y, Lin A, Wang X. The dual-current control strategy of grid-connected inverter with LCL filter. IEEE Transactions on Power Electronics. 2018;34(6):5940-52. 10.1109/TPEL.2018.2869625

22. Zhou X, Zhou L, Chen Y, Shuai Z, Guerrero JM, Luo A, et al. Robust grid-current-feedback resonance suppression method for LCL-type grid-connected inverter connected to weak grid. IEEE Journal of Emerging and Selected Topics in Power Electronics. 2018;6(4):2126-37. 10.1109/JESTPE.2018.2805823

23. He Y, Wang X, Ruan X, Pan D, Qin K. Hybrid active damping combining capacitor current feedback and point of common coupling voltage feedforward for LCL-type grid-connected inverter. IEEE Transactions on Power Electronics. 2020;36(2):2373-83. 10.1109/TPEL.2020.3008160

24. Faiz MT, Khan MM, Jianming X, Ali M, Habib S, Hashmi K, et al. Capacitor voltage damping based on parallel feedforward compensation method for LCL-filter grid-connected inverter. IEEE Transactions on Industry Applications. 2019;56(1):837-49. 10.1109/TIA.2019.2951115

25. Li X, Fang J, Tang Y, Wu X, Geng Y. Capacitor-voltage feedforward with full delay compensation to improve weak grids adaptability of LCL-filtered grid-connected converters for distributed generation systems. IEEE Transactions on Power Electronics. 2017;33(1):749-64. 10.1109/TPEL.2017.2665483

26. Zou C, Liu B, Duan S, Li R, editors. A feedfoward scheme to improve system stability in grid-connected inverter with LCL filter. 2013 IEEE Energy Conversion Congress and Exposition; 2013: IEEE. 10.1109/ECCE.2013.6647299

27. Liu B, Wei Q, Zou C, Duan S. Stability analysis of LCL-type grid-connected inverter under single-loop inverter-side current control with capacitor voltage feedforward. IEEE Transactions on Industrial Informatics. 2017;14(2):691-702. 10.1109/TII.2017.2766890

28. Figueredo RS, Matakas L. Integrated common and differential mode filter with capacitor-voltage feedforward active damping for single-phase transformerless PV inverters. IEEE Transactions

on Power Electronics. 2019;35(7):7058-72. 10.1109/TPEL.2019.2956184

29. Rodriguez-Diaz E, Freijedo FD, Vasquez JC, Guerrero JM. Analysis and comparison of notch filter and capacitor voltage feedforward active damping techniques for LCL grid-connected converters. IEEE Transactions on Power Electronics. 2018;34(4):3958-72. 10.1109/TPEL.2018.2856634

30. Said-Romdhane MB, Naouar MW, Slama Belkhodja I, Monmasson E. An improved LCL filter design in order to ensure stability without damping and despite large grid impedance variations. Energies. 2017;10(3):336. 10.3390/en10030336

Persian Abstract

چکیده

اینورترهای متصل به شبکه به منظور ارتباط موثر منابع انرژی تجدیدپذیر و کاربرد در سیستم تولید پراکنده به عنوان عناصر حیاتی در نظر گرفته می‌شوند. هارمونیک‌های جریان تولید شده ناشی از ریپل در لینک DC و کلیدزنی فرکانس بالا از جمله معایب اینورترهای متصل به شبکه هستند که با استفاده از فیلترهای LCL کاهش می‌یابند. با این وجود، تشدید ذاتی در فیلتر LCL منجر به ناپایداری سیستم انتقال توان می‌شود. در نتیجه، میراسازی مناسب برای حذف تشدید در فیلتر LCL حائز اهمیت می‌باشد. هدف این مقاله، بهبود کیفیت توان تزریقی آرایه فتوولتائیک متصل به شبکه مبتنی بر فیلتر LCL است. بدین منظور، پایداری سیستم اینورتر متصل به شبکه با به کارگیری روش میراسازی فعال بررسی شده و ردیابی نقطه حداکثر توان (MPPT) برای آرایه PV انجام شده است. روش میراسازی فعال پیشخور ولتاژ خازن با در نظر گرفتن تاخیر محاسباتی در این مقاله ارائه شده است. با ترکیب این روش و میراسازی فیدبک جریان سمت اینورتر، کنترل پیشنهادی مشخصات فرکانس پایین سیستم را مستقل از تغییرات امپدانس شبکه حفظ نموده و قابلیت رد هارمونیک بالا را بدون استفاده از جبرانسازهای اضافی فراهم می‌نماید. ولتاژ خازن نیز به عنوان جایگزینی از ولتاژ شبکه برای حلقه قفل فاز (PLL) اندازه‌گیری شده که منجر به کاهش تعداد حسگر شده است. در ضمن ردیابی نقطه حداکثر توان با استفاده از تکنیک هدایت افزایشی (IC) در مبدل بوست پیاده‌سازی شده است. علاوه بر این، روش محاسباتی ساده و مناسب برای طراحی پارامترهای فیلتر LCL ارائه شده و حساسیت سیستم تحلیل شده است. نهایتا، شبیه‌سازی در نرم افزار MATLAB پیاده‌سازی شده است که نتایج حاصله بیانگر عملکرد صحیح و دقیق سیستم کنترلی در تزریق حداکثر توان آرایه فتوولتائیک به شبکه و کیفیت بسیار مطلوب جریان تزریقی به شبکه است.